Wireless Power Transfer

cambridge.org/wpt

Research Article

Cite this article: Moore J, Xu S, Wood BJ, Ren H, Tse ZTH (2020). Radiofrequency tumor ablation system with a wireless or implantable probe. *Wireless Power Transfer* **7**, 95–105. https://doi.org/10.1017/wpt.2020.10

Received: 12 February 2020
Revised: 5 June 2020
Accepted: 23 June 2020
First published online: 12 August 2020

Key words:
Medical devices; radiofrequency ablation; tissue ablation; wireless power transfer

Author for correspondence:
Zion Tsz Ho Tse, Department of Electronic Engineering, University of York, Heslington, York, UK. E-mail: zion.tse@york.ac.uk

Radiofrequency tumor ablation system with a wireless or implantable probe

Julian Moore[1], Sheng Xu[2], Bradford J. Wood[2], Hongliang Ren[3] and Zion Tsz Ho Tse[4]

[1]School of Electrical and Computer Engineering, The University of Georgia, Athens, GA 30602, USA; [2]Center for Interventional Oncology, Radiology and Imaging Sciences, NIH Clinical Center, National Institute of Biomedical Imaging and Bioengineering, and National Cancer Institute Center for Cancer Research, National Institutes of Health, Bethesda, MD, USA; [3]Department of Biomedical Engineering, National University of Singapore, Singapore, Singapore and [4]Department of Electronic Engineering, University of York, Heslington, York, UK

Abstract

Radiofrequency ablation (RFA) is a non-invasive image-guided procedure where tumors are heated in the body with electrical current. RFA procedures are commonly indicated for patients with limited local disease or who are not surgical candidates. Current methods of RFA use multiple cords and wires that ergonomically complicate the procedure and present the risk of cutting or shorting the circuit if they are damaged. A wireless RFA technique based on electromagnetic induction is presented in this paper. The transmitting and receiving coils were coupled to resonate at the same frequency to ensure the highest power output. The receiving coil was connected to two insulated electrodes on a catheter, which allowed the current to flow to the targeted tissue. The prototype system was tested with *ex-vivo* bovine tissue, which has similar thermal and electrical properties to human tissue. The setup can monitor the received power, efficiency, temperature, and ablation zone during ablation procedures. The maximum received power was 15 W, and the average maximum efficiency was 63.27%. The novel system was also able to ablate up to a 2 cm ablation zone in non-perfused tissue. This proof of concept for performing RFA wirelessly with electromagnetic induction may merit further optimization.

Introduction

Thermal ablation procedures can treat various medical problems, including cardiac ablation for arrhythmia treatment, lateral branch neurotomy for chronic sacroiliac joint pain, and localized cancer ablation in the liver [1], kidney, lung, soft tissue, or bone [2–4].

Tissue ablation can destroy cancerous or benign tumors and can be executed less invasively with needle-sized incisions, lower cost, fewer risks, and a shorter recovery. In most modalities, the tissue is heated or cooled to cytotoxic temperatures with several different types of energy. Cryoablation uses extreme cold to ablate, whereas microwave, radiofrequency, high intensity focused ultrasound, and laser ablations use heat to ablate [5–8]. In thermal ablations, temperatures above 60°C will cause destruction at the cellular level, leading to cell death [9].

Radiofrequency ablation (RFA) is often used to treat lesions in the liver, kidney, lung, bone, breast, prostate, and pancreas [10, 11]. During RFA, an electrical current alternates at radiofrequencies between two electrodes [9, 12, 13]. A probe is inserted into the body until it comes into contact with the target tissue. The target tissue introduces resistance, completing a circuit between the two electrodes [14]. The impedance of human tissue is typically within the range of 75–200 Ω [15, 16]. Thus, when current is introduced into tissue in RF tumor ablation procedures, the ions in the tissue align in the direction of the current. When the current alternates, the ions agitate, causing friction and tissue coagulation, which ultimately result in cell death [17, 18].

In terms of the mode of electrode placement, there are two options, monopolar RFA and bipolar RFA. Monopolar RFA inserts one needle or catheter electrode into the body to induce current with another "dispersive electrode," which is a grounding pad on the skin, usually on the thigh. The ablating electrode or electrodes that are inserted into the lesion radiate heat outward fairly uniformly along the lines of current density, because there is a significant distance to the dispersive electrode [19]. Bipolar RFA deploys both electrodes into the body and the currents flow between them. This method ablates the tissue directly between the electrodes in the tissue at the volume of maximum current density. When the electrodes have a similar surface area, the current density in that region will be more uniform. However, if the electrode sizes are unequal or unevenly distributed, and the current remains the same, the current density will be higher around the electrode with the smaller surface area [19, 20].

In practice, there are three methods to perform these RFAs – percutaneously, laparoscopically, or by open laparotomy. Percutaneous ablations are generally outpatient procedures conducted with contrast-enhanced computerized tomography (CT) guidance and occasionally accompanied by live fluoroscopy or ultrasonography. Percutaneous RFA can be performed under general or local anesthesia, whereas laparoscopic and open surgical RFA requires general anesthesia. Ablations performed percutaneously may have less risk for complications, but visualization is sometimes limited [20, 21].

Laparoscopic ablations utilize enhanced imaging with endoscopic cameras and/or ultrasound transducers placed on the surface of the organ. While increased visualization can lead to more accurate staging and ablation, probe placement is difficult since probes must enter through a laparoscopic port. The laparoscopic approach is more invasive than the percutaneous method and may require more hospitalization [21–23]. Open surgical laparotomy RFA is often performed at the same time as resection of larger tumor tissue. In this method, small tumors may be precisely ablated, but it is a more invasive procedure and requires additional recovery time [20, 21].

Microwave ablation (MWA) is an alternative form of thermal ablation to treat cancer using electromagnetic waves in the microwave energy spectrum (300 MHz to 300 GHz) to produce tissue-heating effects [24–30]. However, MWA is out of the scope of this study.

Current percutaneous tumor ablation procedures are usually performed in a procedural room equipped with a cone-beam CT fluoroscopy or CT scanner. These procedural rooms also have anesthesia and patient monitoring equipment. A number of equipment and cables may be tethered to the patient, which may limit the workflow efficiency and ergonomics. The weight of the ablation cables could also alter the needle location when the physician lets go of them, as commonly occurs during CT imaging.

During the procedure, there are multiple people in the operating room, including the interventional radiologist who performs the ablation, one to two imaging technologists, an anesthesiologist, a nurse anesthetist or anesthesia technologist, nurses, and sometimes students, fellows, or trainees. Since the operating room is a bustling environment, it is possible that personnel could trip on cords during procedures.

In the methods presented in this paper, bipolar RFA is utilized; thus, both electrodes are localized and connected to the same probe (a catheter or needle). Additionally, the intended use for this work is for percutaneous procedures. The prototype presented in this paper aims to prove the concept of performing RFA procedures using electromagnetic induction with fewer wires.

Methods

Inductive power transfer theory was used to deliver power to the ablating electrodes wirelessly. Table 1 defines all the symbols used in equations (1)–(6).

The Ampere–Maxwell Law states that electrical current flowing through a coil of wire creates a magnetic field around that wire. In addition, when that electrical current alternates in the wire, there will be an alternating magnetic field (equation (1)) [14, 31–34]:

$$\oint \vec{B} d\vec{l} = \mu_0 \left(I_{enc} + \varepsilon_0 \frac{d}{dt} \int_S \vec{E} \circ \hat{n} da \right) \tag{1}$$

Table 1. Symbols and definitions used in equations (1)–(6)

Symbol	Definition	Unit
B	Magnetic field	T
E	Electrical field	V/m
dl	Length of element	m
μ_0	Permeability of free space	N/A
I_{enc}	Enclosed current	A
ε_0	Electric permittivity of free space	N/A
I	Current	A
R	Radius of the wire	mm
$\hat{n}$	Outward point unit-normal	N/A
Φ_B	Magnetic flux	Wb
ε	Electromotive force	V
$f_{resonant}$	Resonant frequency	Hz
L	Inductance	H
C	Capacitance	F
$SA_{inside\ stylet}$	Surface area of the inner stylet	m^2
$SA_{outside\ sheath}$	Surface area of the outer sheath	m^2
d_{cyl}	Diameter of the cylinder	m
h_{cyl}	Height of the cylinder	m
d_{cone}	Diameter of the cone	m
h_{cone}	Height of the cone	m

The Law of Biot–Savart (equation (2)) is applied to determine the magnetic field [14, 31–34]:

$$B = \frac{\mu_0 I}{4\pi R^2} \oint dL = \frac{\mu_0 I}{2R} \tag{2}$$

Faraday's Law of induction states that an electromotive force will be induced on a coil of wire placed into a changing magnetic field. This law represents the relationship between the strength of the magnetic field (flux), the area of the coil, and the number of turns in that coil (equation (3)) [31–34]:

$$\varepsilon = -N \frac{\Delta \Phi_B}{\Delta t} \tag{3}$$

The frequency of the oscillations can be modified by changing the inductance of the coil or the capacitance of its tuning capacitor in the LC tank circuit. The receiving coil has a similar LC tank circuit to the transmitting circuit. The inductors and capacitors are tuned to be in resonance with each other. Magnetic resonance relates the operating frequency to the values of the capacitor and inductor used. When the LC circuit operates at the resonant frequency, its reactance is at its highest point, and its impedance is at its lowest point. Therefore, the power at the resistive load will be high. The formula to determine the resonant frequency in this parallel tank circuit is shown in equation (4) [31–34]:

$$f_{resonant} = \frac{1}{2\pi\sqrt{LC}} \tag{4}$$

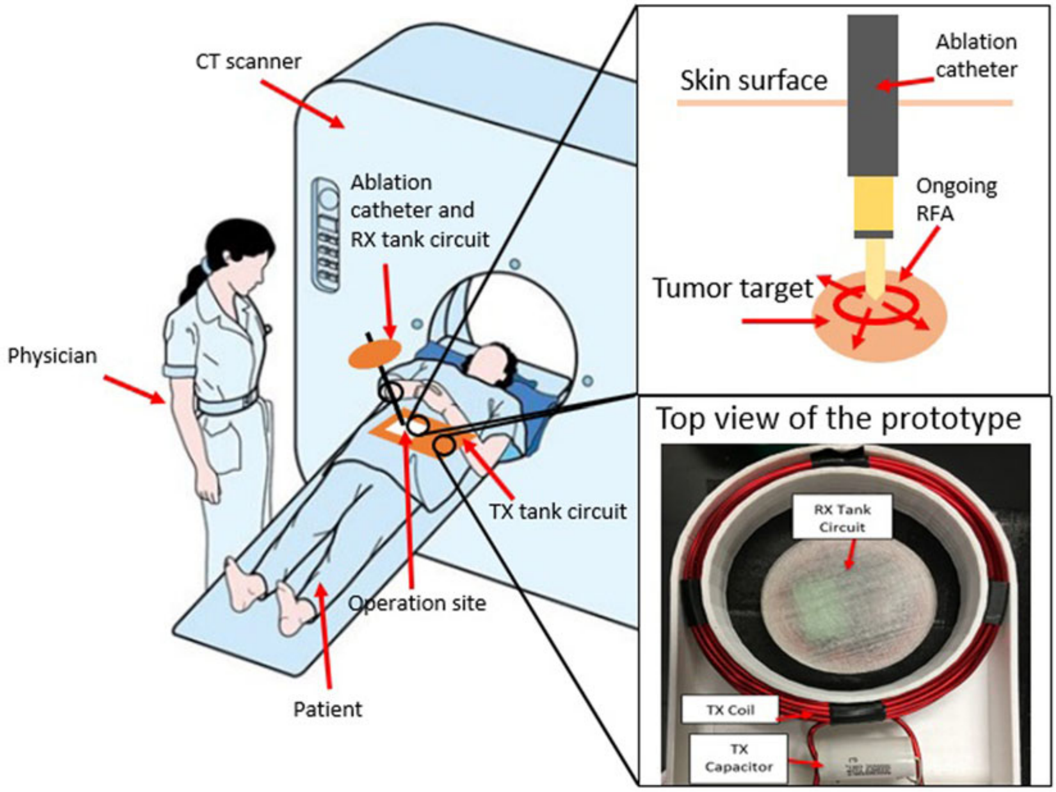

Fig. 1. Schematic diagram of the wireless ablation system. The wireless catheter consists of the RX tank circuit.

The ablation system is comprised of two parts: the ablation generator, which has an oscillating circuit, and the transmitting coil. The wireless catheter has the receiving coil and the catheter that is intended to be inserted into the body to ablate the target tissue. The ablation generator creates a magnetic field, and the wireless catheter is placed into that field. Figure 1 shows how the two parts of the system are used together.

Figure 2 shows how the presented system was mounted onto the skin surface.

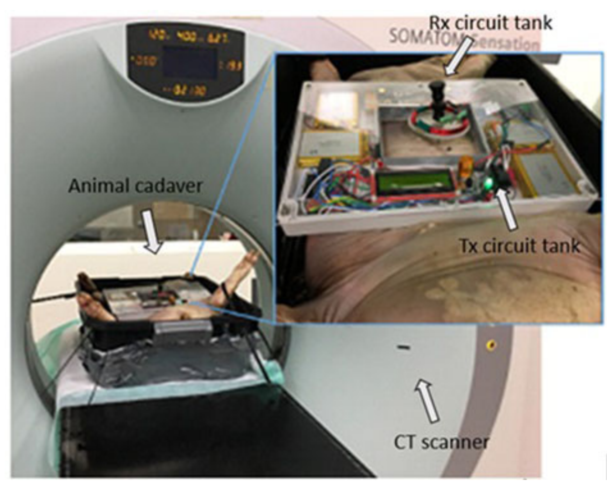

Fig. 2. System mounted on top of an animal cadaver.

Ablation generator

The ablation generator uses an amplification circuit to create an alternating current through a coil to create an alternating magnetic field. A modified Royer amplifier was used to create a medium power alternating current. The Royer amplifier is advantageous when the coil distances are intended to be changed because the oscillation frequency is related to the resonant frequency of the transmitting and receiving tank circuits. Therefore, the oscillating frequency will change as the coil distance varies.

The amplifier utilizes two MOSFETS that are cross-coupled and connected to the LC tank circuit. Once the gate of one of the MOSFETS is triggered, it opens its switch and allows current to flow from the drain to the source. This also forces the gate voltage of the other MOSFET to zero, which turns that switch off, thus only allowing one MOSFET to be on at one time [31]. Figure 3 shows the gate voltage (V_{GS}) of one MOSFET and the drain voltage (V_{DS}) of the cross-coupled MOSFET.

The circuit is powered using a 12–24 V adjustable power supply with a maximum DC current of 2.5 A. The LC tank circuit is designed in a parallel configuration with its characteristics defined in Table 2. With equation (4) and the values of the LC tank circuit, a frequency of 50.5 kHz is calculated. This value was validated in practice as an oscillating frequency of 50–55 kHz was observed. This circuit amplifies the natural oscillating feedback of the LC tank circuit to create a strong magnetic field through the coil [35, 36]. Figure 4 shows the diagram of the modified Royer circuit used to amplify the oscillations of the tank.

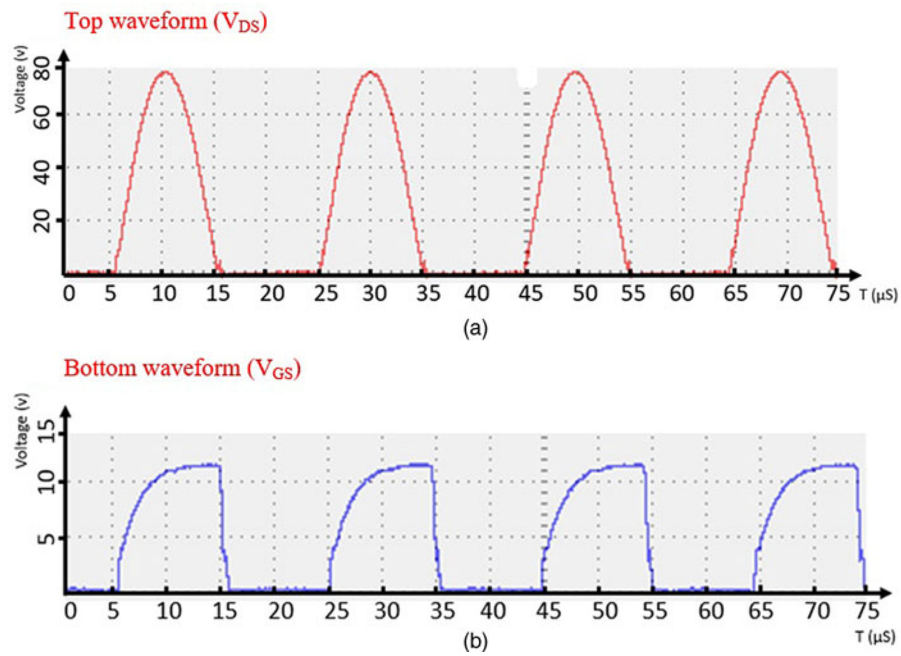

Fig. 3. Time-domain analysis of V_{GS} and V_{DS} of the cross-coupled MOSFET: (a) the top waveform (V_{DS}) and (b) the bottom waveform (V_{GS}) of the cross-coupled MOSFET.

Table 2. TX and RX tank circuit characteristics

TX tank circuit		RX tank circuit	
Variable	Value	Variable	Value
Inductance	25.74 µH	Inductance	25.69 µH
Capacitance	386.3 nF	Capacitance	400.2 nF
Coil diameter	10 cm	Coil diameter	5 cm
Coil turns	12	Coil turns	14

Wireless catheter

While the ablation generator produces an oscillating magnetic field, the receiving coil connected to the wireless catheter is placed within those flux lines, and a voltage is induced (equation (3)). The receiving LC tank circuit is half the diameter of the transmitting and has a parallel configuration that is in resonance with the transmitting circuit (Table 2; Fig. 5).

The prototype probe (needle/catheter) used in this work is 6.5 gage and 12 cm in length. The device is composed of two parts: the inside stylet and the outside sheath. Each part is connected to one side of the receiving LC circuit, as shown in Fig. 6. These two parts are insulated from each other in order to only allow current to flow from the electrodes through the load.

The surface area of the electrodes is critical to consider in order to predict and understand the ablation zone the catheter creates. The geometry of the inside stylet electrode is composed of a hollow cylinder and a cone. Therefore, the surface area of this electrode is represented by equation (5). The surface area of the inside stylet electrode was calculated to be 67 mm^2:

$$SA_{inside\ stylet} = \pi d_{cyl} h_{cyl} + \frac{\pi d_{cyl}}{2}\sqrt{\left(\frac{d_{cone}}{2}\right)^2 + (h_{cone})^2} \qquad (5)$$

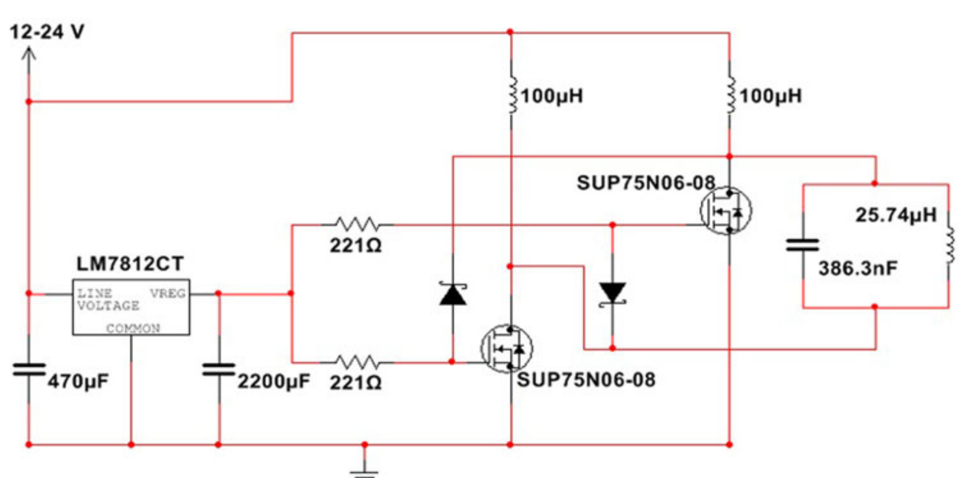

Fig. 4. Circuit diagram of the transmitting (TX) circuit.

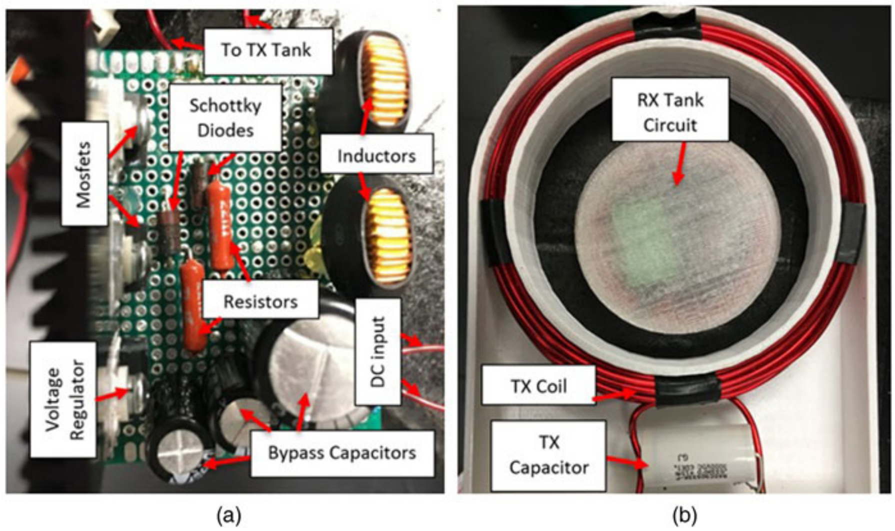

Fig. 5. Photo of (a) the TX circuit and (b) the TX and RX tank circuit.

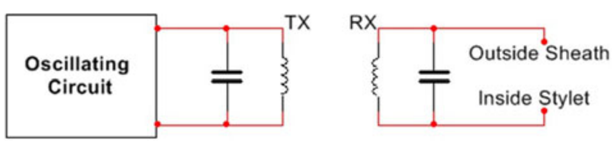

Fig. 6. Diagram of the transmitting (TX) and receiving (RX) circuits.

The geometry of the outside sheath electrode is composed of a hollow cylinder and its circular base, which is represented as an annulus. Therefore, the surface area of this electrode is represented by equation (6). The surface area of the outside sheath electrode was calculated to be 79 mm^2:

$$SA_{outside\ sheath} = \pi d_{cyl} h_{cyl} + \pi\left(\left(\frac{d_1}{2}\right)^2 - \left(\frac{d_2}{2}\right)^2\right) \qquad (6)$$

The catheter was constructed so that the surface area of the outside sheath electrode was 18% greater than the inside stylet electrode surface area. This difference in surface areas directs the ablation zone toward the electrode with the smallest electrode surface area [19, 37]. In this case, the electrode with the smaller surface area is the inside stylet electrode; therefore, the ablation zone is closer to the tip of the coaxial probe system (Fig. 7).

A thermistor is also inserted into the hollow catheter to measure the temperature at the tip of the catheter during ablation. The thermistor is connected to a small battery-powered circuit that allows the catheter to be completely independent of any wired source. The thermistor is modified from a commercially available thermometer, Delta Track 11063 [38]. The probe has a length of 99 mm and a diameter of 1.6 mm. The accuracy is 0.1°C.

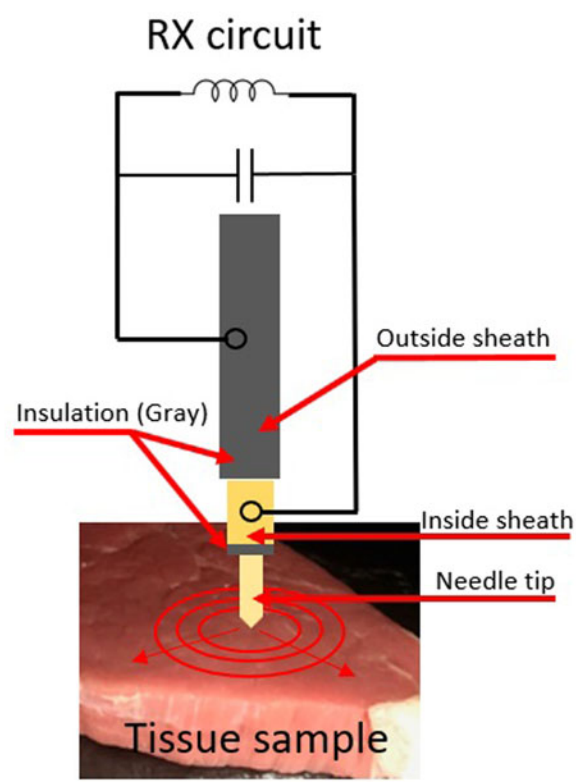

Fig. 7. Shows how the Rx tank circuit is connected with the ablation electrode.

Experimental results

Four experiments were performed to evaluate the performance of the wireless ablation system. The first and second tests directly focused on the efficiency of the wireless power transfer. A resistor was connected to the RX coil, and power was measured as the distance between the coils increased, and as the input, DC voltage changed. Then, the third test was to ablate *ex-vivo* bovine tissue to evaluate the feasibility of this ablation system. For these experiments, the wireless catheter was connected in parallel to a load, either a resistor or animal tissue. This setup is represented by the circuit diagram found in Fig. 8.

Coil distance and power efficiency with resistive load

The power of the ablation system was measured at the transmitting and receiving side to determine the efficiency of the wireless power transfer while the distance between the coils increased.

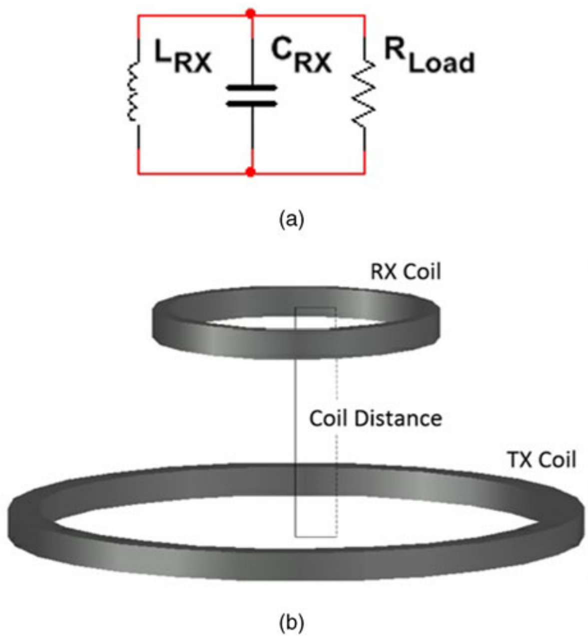

Fig. 8. Diagram of the receiving (RX) circuit during testing and ablation: (a) circuit diagram and (b) schematic diagram.

In this experiment, a purely resistive load was added in parallel with the receiving tank circuit. The resistor was measured to be 103.1 Ω. We recorded the power received and its corresponding power efficiency at each coil distance. As the insertion depth increased, the distance between the coils decreased.

These tests were performed using a DC input voltage of 24 VDC, where the maximum transmitting power was possible. Three trials were conducted when the RX coil was at 0, 30, and 40° with the TX coil, respectively. The average standard deviation for the RX power is ±1.8 W for the three trials. The average standard deviation for power efficiency is ±4.9% for the three trials (Fig. 9).

The largest received power and efficiency were achieved when the coils were within the transmission range. A maximum of 15 W was recorded at the load. As the coil distance increased, the received power and efficiency decreased. The minimum desired RX power was 3 W. Powers less than this take an extremely long time to ablate with the presented catheter. Thus, a 6 cm coil distance was indicated as the maximum working distance.

Received power and varying DC input voltage with resistive load

When the presented ablation system is in use, the only variables able to be manipulated are the probe insertion depth and the DC input voltage. This experiment aimed to determine the received power and the corresponding power efficiency as the DC input voltage varied. The operational voltage for the DC input ranged from 12 to 24 VDC. In this experiment, the power and efficiency were measured at increments of 1 VDC. The resistor was measured to be 103.1 Ω.

Since the coils remained within the transmission range during these tests, the mutual inductance of the two tank circuits also stayed the same. Again, three trials were conducted in this test, the RX coil was in 0, 30, and 40° with the TX coil, respectively. The average standard deviation was ±7.6 W. In trial #1(i) of Fig. 10, the power received increased linearly as the DC input voltage increased. The average standard deviation was ±1.4% for the three trials. The average power efficiency was 63.27% for the three trials.

Ex-vivo *bovine tissue experiment*

In this experiment, *ex vivo* bovine tissue was ablated with the custom fabricated ablation system (Fig. 11). Two tests were conducted – one with maximum ablation power, and one with minimum ablation power. The temperature was recorded with the thermistor circuit on the wireless catheter. This tissue had an initial impedance of about 175 Ω for all tests. The temperature of the tissue was monitored while the ablations were performed.

Maximum power

The first test was ablation at 24 VDC with the coils within the transmission distance. Three trials were conducted for 2 min, and the temperatures during ablations were plotted over time (Fig. 12(b)). The error line was plotted based on the measurement of the three trials. The average standard deviation for this test was ±2.21°C, which was insignificant compared to the average temperature. From these data, consistent temperature rise and decay were observed for each trial. The ablation zones were also nearly the same, with a width of 9 mm, and a length of 18 mm (Fig. 12(a)).

Minimum power

The next test was ablating the tissue at its minimum powers. This was achieved with an input voltage of 12 VDC at 0 cm coil distance and an input voltage of 24 VDC at 6 cm coil distance. The tissue was ablated for 5 min in each case, and their temperatures during ablation were plotted over time (Fig. 13(b)). One measurement was taken in each case. From the temperature data, the 12 VDC ablation had a faster rise in temperature because the power was slightly higher. The ablation at 6 cm distance had a lower power because the temperature rise was slower. However, the ablation zones for both tests were nearly the same, with a width of 12 mm and a length of 21 mm.

Conclusions

Ablation therapy has become a widely practiced technique for targeted image-guided focal ablation of both cancerous and benign tissue. Tumor ablation can be achieved with many types of energy by bringing the tissue above the cytotoxic temperature of 60°C. RFA uses alternating electrical current to ablate tissue by ionic agitation.

A custom bipolar RFA system was developed to investigate the possibility of ablating tissue wirelessly. The system was composed of an ablation generator and a wireless probe (coaxial needle/catheter). The generator was composed of an oscillating circuit that created a medium power magnetic field. The catheter had a receiver coil that was induced with a voltage when placed in the magnetic field. The catheter had two electrodes that allowed the alternating current to flow through tissue, achieving tissue destruction.

The performance of this ablation system was evaluated in terms of its received power, temperature, and ablation size. The average maximum received power was 15 W, and the average maximum efficiency was 63.27%. The ablation power and

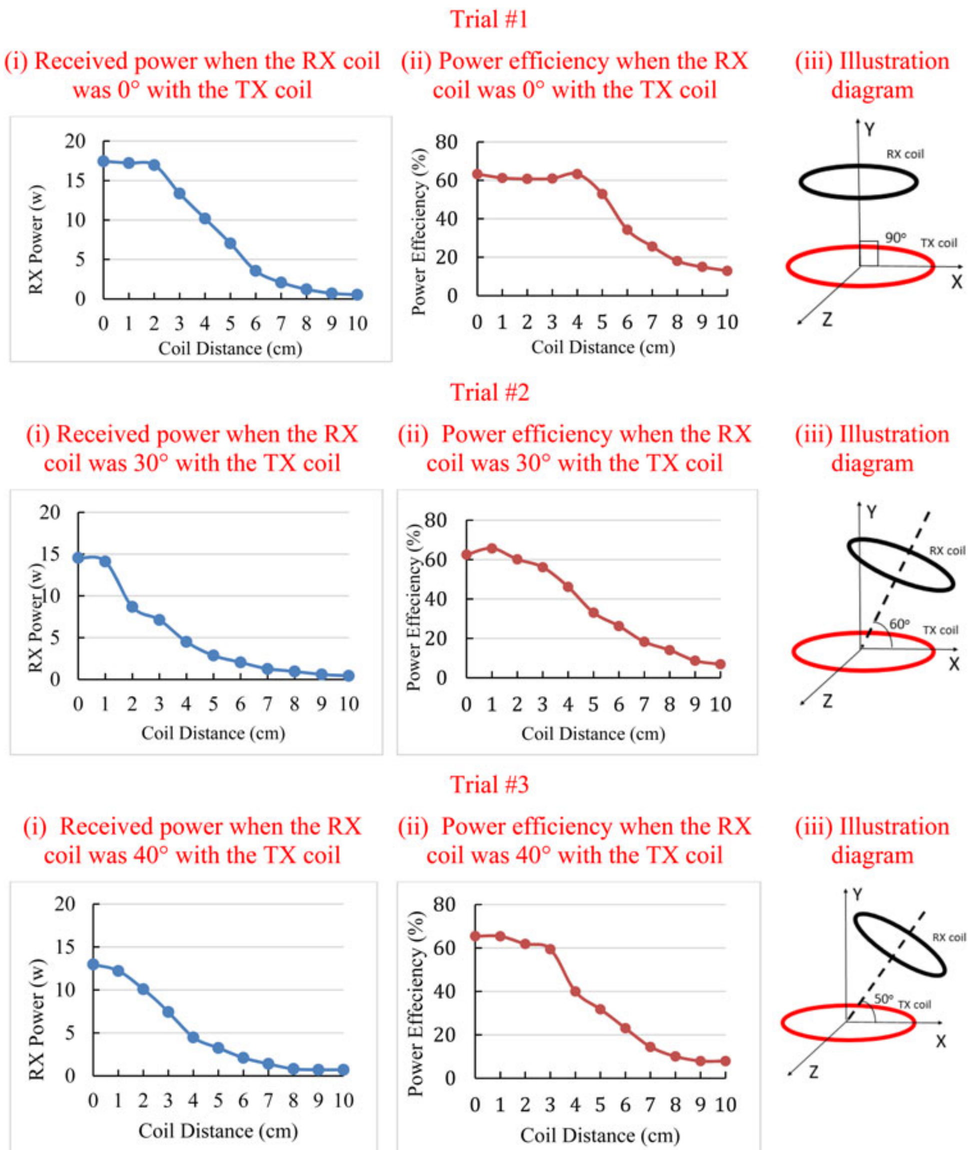

Fig. 9. Shows the trend of received power as well as power efficiency with respect to the coil distance in three different trials, trail #1 is conducted when the RX coil is in parallel with the TX coil. (i) Shows the relationship between the received power and the coil distance. The dotted line is the minimum desired RX power. The received power is above the minimum requirement of 2.5 W when the coil distance is less or equal to 6 cm. (ii) Shows the relationship between power efficiency and coil distance, and (iii) shows the orientation of the RX coil (black) with respect to the TX coil (red).

temperature were tested using *ex-vivo* bovine tissue. The system was able to ablate up to an ablation zone with a diameter of 12 mm, which is a clinically relevant size. Focused ultrasound, as an alternative modality, could generate a uniform cylindrical ablation profile with a diameter of 1–3 mm and length of 2–5 mm [39].

With these results, the concept of using inductive power transfer to perform RFA wirelessly was proven, even prior to optimization or refinement. The prototype ablation system outlined in this study proved the concept, rationale, and feasibility of wireless ablation. Design and system modifications, as well as system miniaturization, may further improve the system. The efficiency of power transfer can be increased by using a more robust amplifier with lower resistive losses. Additionally, more tuning may be needed in order to increase the coupling between the two coils. Further experiments could be conducted to evaluate the size of the ablation zone with electrodes of different surface areas and spacing.

Moreover, three more tests will be performed for the characterization of this prototype. One test is to measure the dependency of the received power and power efficiency based on different values of the load. Another test is to measure the power efficiency with respect to DC voltage input at specific insertion depth, i.e. coil distance. The final test is to measure the temperature variation of the catheter tip with respect to the ablation time at specific coil distance.

The exact clinical utility remains to be defined, but it could simplify thermal ablations where the probe must be left unattended, such as during CT scanning. Although extremely speculative at present, another application might also include settings wherein intermittent and non-invasive heating is desired, whereby such coaxial electrodes might be semi-permanently

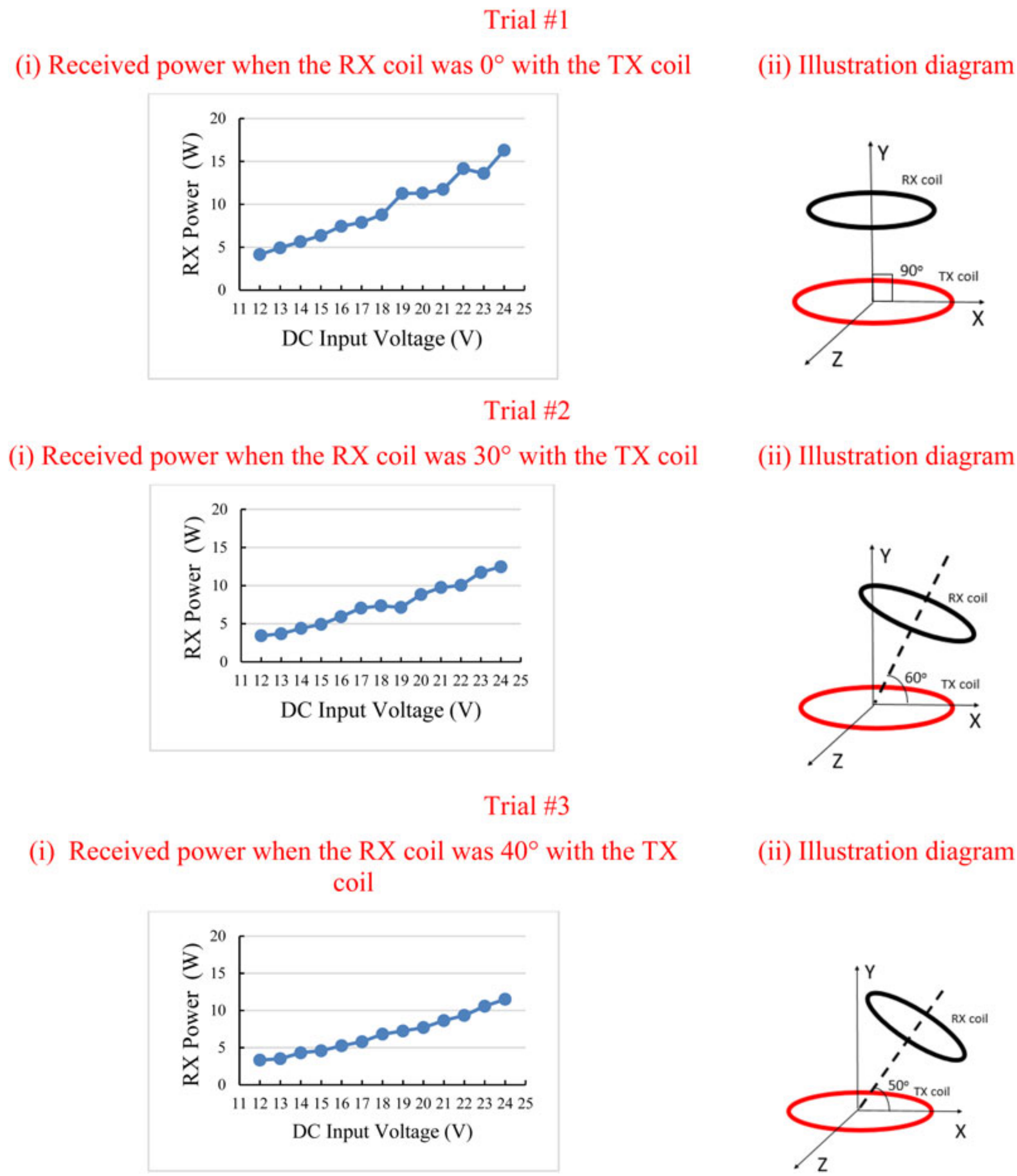

Fig. 10. Shows the trends of received power and efficiency with respect to the DC input voltage in the trials #1–3. Trail #1 is conducted when the RX coil is in parallel with the TX coil. (i) Shows the relationship between the received power and the coil distance. The received power was all above the minimum requirement of 2.5 W for the whole test. (ii) Shows the orientation of the RX coil (black) with respect to the TX coil (red).

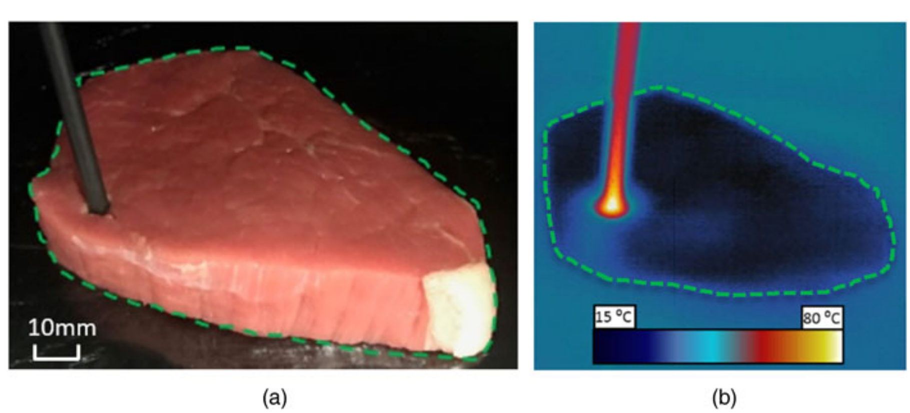

Fig. 11. Setup of the bovine liver experiment: (a) *ex vivo* bovine tissue during ablation and (b) thermal image during ablation.

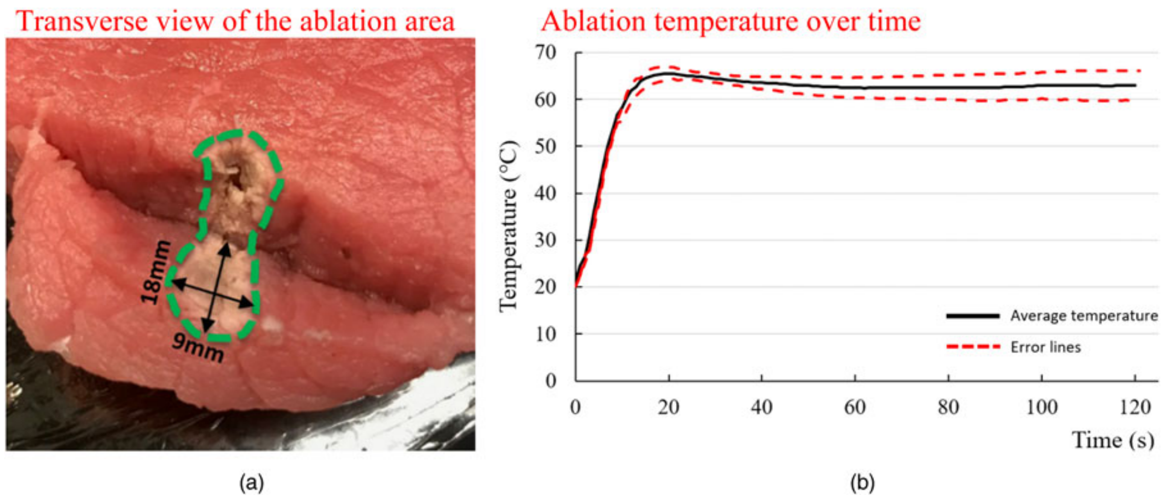

Fig. 12. Results of maximum power test: (a) cross-section of ablation zone (9 mm × 18 mm) and (b) ablation temperatures over time. The black line represents the average temperature. The dotted red lines represent the error lines calculated using standard deviation.

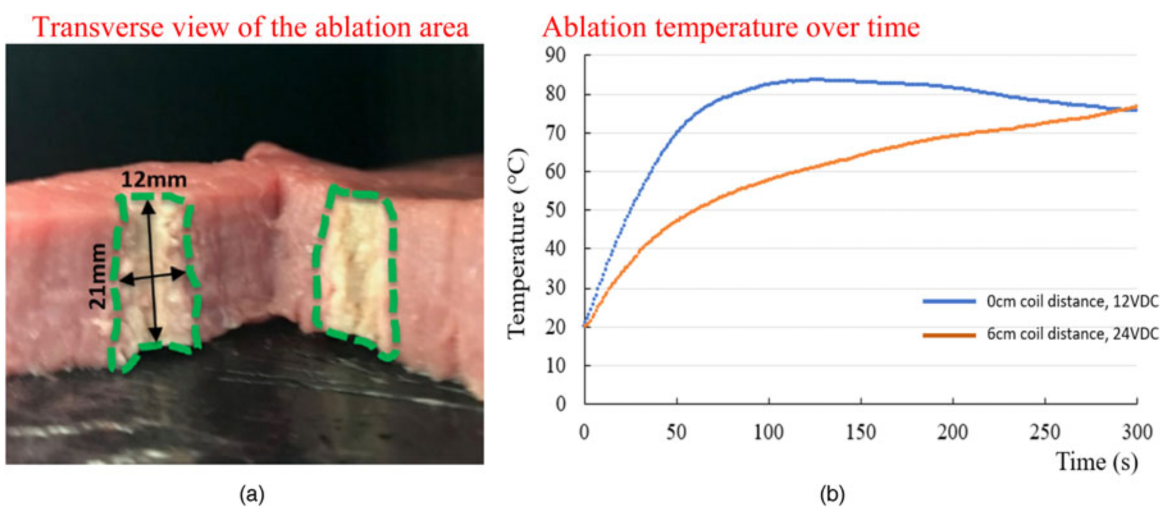

Fig. 13. Results from the minimum power test: (a) cross-section of ablation zone (12 mm × 21 mm) and (b) ablation temperatures over time. The blue line represents the average temperature when the coil distance is 0 cm, and voltage is 12 VDC, the light brown line represents the average temperature when the coil distance is 6 cm, and the voltage is 24 VDC.

placed with image guidance at target tissues for subsequent and sequential stimulation of indwelling wireless fiducial probes, such as for nerve stimulation, immunomodulation, or radiation sensitization. The absence of wires could be a design advantage in specific settings.

Acknowledgements. Rui Li has provided professional advice and editing in the manuscript to enhance the scientific content and readability.

Financial support. This project is sponsored by the NIH Center for Interventional Oncology grant. This study was also supported in part by the National Institutes of Health (NIH) Bench-to-Bedside Award, the NIH Center for Interventional Oncology Grant, the National Science Foundation (NSF) I-Corps Team Grant (1617340), NSF REU site program 1359095, the UGA-AU Inter-Institutional Seed Funding, the American Society for Quality Dr. Richard J. Schlesinger Grant, the PHS Grant UL1TR000454 from the Clinical and Translational Science Award Program, the NIH National Center for Advancing Translational Sciences, and Singapore Academic Research Fund under TAP Grant R397000350118/Skullbot.

Conflict of interest. The authors have no conflicts of interest. NIH does not endorse or recommend any commercial products, processes, or services. The views and opinions of authors expressed herein do not necessarily state or reflect those of the U.S. Government, nor does it constitute policy, endorsement or recommendation by the U.S. Government or National Institutes of Health (NIH). Please reference to the U.S. Code of Federal Regulations or U.S. Food and Drug Administration for further information.

References

1. **Ren H, Campos-Nanez E, Yaniv Z, Banovac F, Abeledo H, Hata N and Cleary K** (2013) Treatment planning and image guidance for radiofrequency ablations of large tumors. *IEEE Journal of Biomedical and Health Informatics* **18**(3), 920–928.
2. **Blessing E, Esler MD, Francis DP and Schmieder RE** (2013) Cardiac ablation and renal denervation systems have distinct purposes and different technical requirements. *JACC: Cardiovascular Interventions* **6**(3), 314.
3. **Pandina GJ, Lindenmayer JP and Lull J and Lim P and Gopal S and Herben V and Kusumakar V and Yuen E and Palumbo J** (2012) A

randomized, placebo-controlled study to assess the efficacy and safety of 3 doses of paliperidone palmitate in adults with acutely exacerbated schizophrenia. *Journal of Clinical Psychopharmacology* **30**(3), 235–244.
4. **Joo Y-C, Park J-Y and Kim K-H** (2013) Comparison of alcohol ablation with repeated thermal radiofrequency ablation in medial branch neurotomy for the treatment of recurrent thoracolumbar facet joint pain. *Journal of Anesthesia* **27**(3), 390–395.
5. **Livraghi T, Goldberg SN, Lazzaroni S, Meloni F, Solbiati L and Gazelle GSJR** (1999) Small hepatocellular carcinoma: treatment with radio-frequency ablation versus ethanol injection. *Radiology* **210**(3), 655–661.
6. **Pearson AS, Izzo F, Fleming RD, Ellis LM, Delrio P, Roh MS, Granchi J and Curley SA** (1999) Intraoperative radiofrequency ablation or cryoablation for hepatic malignancies. *The American Journal of Surgery* **178**(6), 592–598.
7. **Souchon R, Rouvière O, Gelet A, Detti V, Srinivasan S, Ophir J and Chapelon JY** (2003) Visualisation of HIFU lesions using elastography of the human prostate in vivo: preliminary results. *Ultrasound in Medicine and Biology* **29**(7), 1007–1015.
8. **Vogel A and Venugopalan VJCR** (2003) Mechanisms of pulsed laser ablation of biological tissues. *Chemical Reviews* **103**(2), 577–644.
9. **Brace CL** (2009) Radiofrequency and microwave ablation of the liver, lung, kidney, and bone: what are the differences? *Current Problems in Diagnostic Radiology* **38**(3), 135–143.
10. **Curley SA** (2003) Radiofrequency ablation of malignant liver tumors. *Annals of Surgical Oncology* **10**(4), 338–347.
11. **Mirza AN, Fornage BD, Sneige N, Kuerer HM, Newman LA, Ames FC and Singletary SE** (2001) Radiofrequency ablation of solid tumors. *Cancer Journal (Sudbury, Mass.)* **7**(2), 95–102.
12. **Goldberg SN, Gazelle GS, Solbiati L, Rittman WJ and Mueller PR** (1996) Radiofrequency tissue ablation: increased lesion diameter with a perfusion electrode. *Academic Radiology* **3**(8), 636–644.
13. **Haines DE** (1993) The biophysics of radiofrequency catheter ablation in the heart: the importance of temperature monitoring. *Pacing and Clinical Electrophysiology* **16**(3), 586–591.
14. **Moore J, Nilsson KR, Wood B, Xu S and Tse ZTH** (2018) Liver radiofrequency ablation using wirelessly powered catheter and generator. in 2018 IEEE PELS Workshop on Emerging Technologies: Wireless Power Transfer, Wow 2018, Montreal, Canada, July 2018: Institute of Electrical and Electronics Engineers Inc.
15. **Haemmerich D** (2010) Biophysics of radiofrequency ablation. *Critical Reviews in Biomedical Engineering* **38**(1), 1–16.
16. **Morimoto T, Kimura S, Konishi Y, Komaki K, Uyama T, Monden Y, Kinouchi DY and Iritani DT** (1993) A study of the electrical Bio-impedance of tumors. *Journal of Investigative Surgery* **6**(1), 25–32.
17. **Haemmerich D** (2010) Mathematical modeling of impedance controlled radiofrequency tumor ablation and ex-vivo validation. in Engineering in Medicine and Biology Society (EMBC), 2010 Annual International Conference of the IEEE, IEEE, pp. 1605–1608.
18. **Haemmerich D, Staelin T, Tungjitkusolmun S, Lee FT, Mahvi DM and Webster JG** (2001) Hepatic bipolar radio-frequency ablation between separated multiprong electrodes. *IEEE Transactions on Biomedical Engineering* **48**(10), 1145–1152.
19. **Nakada SY, Jerde TJ, Warner TF, Wright AS, Haemmerich D, Mahvi DM and Lee Jr. FT** (2003) Bipolar radiofrequency ablation of the kidney: comparison with monopolar radiofrequency ablation. *Journal of Endourology* **17**(10), 927–933.
20. **Decadt B and Siriwardena AK** (2004) Radiofrequency ablation of liver tumours: systematic review. *The Lancet Oncology* **5**(9), 550–560.
21. **McGahan JP and Dodd III G** (2001) Radiofrequency ablation of the liver: current status. *American Journal of Roentgenology* **176**(1), 3–16.
22. **Boeti MPS, Grigorie RZ and Popescu I** (2013) Laparoscopic radiofrequency ablation of liver tumors. *Hepatic Surgery*. Available at https://www.intechopen.com/books/hepatic-surgery/laparoscopic-radiofrequency-ablation-of-liver-tumors.
23. **Machi J, Uchida S, Sumida K, Limm WM, Hundahl SA, Oishi AJ, Furumoto NL and Oishi RH** (2001) Ultrasound-guided radiofrequency thermal ablation of liver tumors: percutaneous, laparoscopic, and open surgical approaches. *Journal of Gastrointestinal Surgery* **5**(5), 477–489.
24. **Simon CJ, Dupuy DE and Mayo-Smith WW** (2005) Microwave ablation: principles and applications. *Radiographics* **25**(suppl_1), S69–S83.
25. **Meloni MF, Chiang J, Laeseke PF, Dietrich CF, Sannino A, Solbiati M, Nocerino E, Brace CL and Lee Jr. FT** (2017) Microwave ablation in primary and secondary liver tumours: technical and clinical approaches. *International Journal of Hyperthermia* **33**(1), 15–24.
26. **Hoffmann R, Rempp H, Keßler DE, Weiß J, Pereira PL, Nikolaou K and Clasen S** (2017) MR-guided microwave ablation in hepatic tumours: initial results in clinical routine. *European Radiology* **27**(4), 1467–1476.
27. **Lachenmayer A, Tinguely P, Maurer MH, Frehner L, Knöpfli M, Peterhans M, Weber S, Dufour JF, Candinas D and Banz V** (2019) Stereotactic image-guided microwave ablation of hepatocellular carcinoma using a computer-assisted navigation system. *Liver International* **39**(10), 1975–1985.
28. **Dou J-P, Liang P and Yu J** (2016) Microwave ablation for liver tumors. *Abdominal Radiology* **41**(4), 650–658.
29. **Sidoff L and Dupuy DE** (2017) Clinical experiences with microwave thermal ablation of lung malignancies. *International Journal of Hyperthermia* **33**(1), 25–33.
30. **Wu X, Liu B and Xu B** (2016) Theoretical evaluation of high frequency microwave ablation applied in cancer therapy. *Applied Thermal Engineering* **107**, 501–507.
31. **Agbinya JI** (2015) *Wireless Power Transfer*. Gistrup, Denmark: River Publishers.
32. **Kim KY** (2012) Wireless power transfer-principles and engineering explorations.
33. **Stielau OH and Covic GA** (2000) Design of loosely coupled inductive power transfer systems. in PowerCon 2000. 2000 International Conference on Power System Technology. Proceedings (Cat. No. 00EX409), vol. 1: IEEE, pp. 85–90.
34. **William BT** (1995) *Advanced Electromagnetism: Foundations: Theory and Applications*. New Jersey, USA: World Scientific Publishing Co., Inc.
35. **Costanzo A, Dionigi M, Mastri F and Mongiardo M** (2013) Rigorous modeling of mid-range wireless power transfer systems based on Royer oscillators. in 2013 IEEE Wireless Power Transfer (WPT), IEEE, pp. 69–72.
36. **Mastri F, Costanzo A, Dionigi M and Mongiardo M** (2012) Harmonic balance design of wireless resonant-type power transfer links. in 2012 IEEE MTT-S International Microwave Workshop Series on Innovative Wireless Power Transmission: Technologies, Systems, and Applications, IEEE, pp. 245–248.
37. **Kovoor P, Daly M, Pouliopoulos J, Dewsnap MB, Eipper V and Ross DL** (2005) Effect of inter-electrode distance on bipolar intramural radiofrequency ablation. *Pacing and Clinical Electrophysiology* **28**(6), 514–520.
38. **DeltaTrak.** "FlashCheck® Jumbo Display Auto-Cal Needle Probe Thermometer." DeltaTrak. Available at https://www.deltatrak.com/digital-min-max-thermometers/11063-flashcheck-jumbo-display-auto-cal-needle-probe-thermometer (accessed 4-3-2020, 2020).
39. **Council NR** (1996) *Mathematics and Physics of Emerging Biomedical Imaging*. Washington, D.C: National Academies Press.

Julian Moore obtained his graduate and undergraduate education in electrical engineering at the University of Georgia. He is currently working at the Johns Hopkins University Applied Physics Laboratory in Maryland.

Sheng Xu is the head scientist of the Center for Interventional Oncology at the National Institutes of Health. He obtained his PhD from the Department of Computer Science in the Johns Hopkins University. Then he worked at Philips Research North America for 6 years before he joined NIH. Dr. Xu is interested in surgical navigation, medical image processing, medical robotics and machine learning.

Bradford Wood has practiced and performed translational research at NIH for the past 18 years with the goal of combining drugs devices, and image guidance to meet clinical needs. As an academic interventional radiologist, he defines clinical scenarios where combining image guidance and energy and drug deposition may lead to improved outcomes for cancer patients. He is the first to treat kidney cancer, lymphoma, adrenocortical carcinoma, and pheochromocytoma with radiofrequency ablation, first to combine heat deployed nanoparticle chemotherapy with RFA or HIFU thermal ablation, and first to use fusion guidance for biopsy and thermal ablation. He directs a multidisciplinary research team networking with the NIH institutes while partnering with drug device and pharma industry as well as extramural academic centers in the US and Europe.

Dr. Hongliang Ren is an IEEE senior member and currently serves as an associate editor for IEEE Transactions on Automation Science & Engineering (T-ASE) and Medical & Biological Engineering & Computing (MBEC). He has navigated his academic journey through Chinese University of Hong Kong, Johns Hopkins University, Children's Hospital Boston, Harvard Medical School, Children's National Medical Center, United States, and National University of Singapore. His areas of interest include biorobotics, intelligent control, medical mechatronics, soft continuum robots, soft sensors, and multisensory learning in medical robotics. He is the recipient of NUS Young Investigator Award and Engineering Young Researcher Award, IAMBE Early Career Award 2018, Interstellar Early Career Investigator Award 2018, and ICBHI Young Investigator Award 2019.

Zion Tsz Ho Tse received his PhD in mechatronics in medicine from Imperial College London. Currently he is a chair professor at Department of Electronic Engineering and the principal investigator of the Medical Robotics Lab at University of York, UK. Before joining University of York, he was an associate professor in University of Georgia, USA. Dr. Tse has been involved in designing and prototyping a broad range of novel analog-digital electronic devices, most of which have been applied in numerous clinical and industrial environments.